Characterisation of calcined raw clays suitable as supplementary cementitious materials

Authors:

Tobias Danner, Geir Norden, Harald Justnes

[a] NTNU – Norwegian University of Science and Technology, Department of structural Engineering, Richard Birkelandsvei 1a, 7491 Trondheim

[b] SINTEF Building and infrastructure, Richard Birkelandsvei 3, 7491 Trondheim

[c] Saint-Gobain Weber, 216 Alnabru, 0614 Oslo

Abstract:

The potential use of two raw clays (Clay A: kaolin; Clay B: calcareous montmorillonite) as supplementary cementitious material (SCM) in blended cements was investigated. Cement replacement in mortars by 20% calcined Clay A and Clay B resulted in a considerable 28 day compressive strength improvement. The pozzolanic reactivity of Clay A and B is explained by characterization of the structural changes upon calcination with XRD, ICP-MS, FT-IR, 27Al-NMR, Mössbauer spectroscopy and SEM. At the temperature giving highest pozzolanic reactivity, kaolinite and montmorillonite were completely dehydroxylated, while calcite from Clay B was not completely decomposed. FT-IR, 27Al-NMR and Mössbauer spectroscopy revealed considerable structural deformations of kaolinite in Clay A and montmorillonite in Clay B resulting in an amorphous, reactive state. Oxidation of iron in Clay B during calcination contributed to strong distortions of the octahedral sheet in the montmorillonite structure. Additionally, the formation of a glass phase due to reaction of coccoliths ($CaCO_3$) and montmorillonite was observed.

Key words: pozzolan, cement, coccolith, Mössbauer spectroscopy

Highlights:

- Calcination of raw calcerous montmorillonite can provide a reactive pozzolanic source for environmentally friendly binders with improved compressive strength.
- Oxidation of Fe^{2+} to Fe^{3+} in montmorillonite leads to structural disordering and thus to a higher pozzolanic reactivity.
- Finely intermixed coccoliths in montmorillonite enable the formation of a reactive glass.

1. Introduction

Cement production is a highly energy intensive process, contributing to about 5-7% of the worldwide carbon dioxide emissions (Ernst Worrell et al., 2001; Mehta, 1999). The biggest step towards reducing CO_2 emissions in the short and long term can be achieved by replacing parts of the cement clinker with supplementary cementitious materials (SCMs) (Damtoft et al., 2008; Ernst Worrell et al., 2001; Schneider et al., 2011). In the long run, the right choice of SCM's is mainly a question of availability (Gartner, 2004), as well as pozzolanic reactivity. Natural pozzolans, especially raw clays are widespread and the most promising source of SCM to serve the cement industry sufficiently for a more sustainable future. Since there is a growing interest of applying calcined clays in the construction industry, many countries started to evaluate the pozzolanic potential of local clay deposits (Al-Rawas et al., 2001; Alujas et al., 2015; Aras et al., 2007; Berriel et al., 2016; Beuntner and Thienel, 2015; Chakchouk et al., 2006; Huenger et al., 2018; Shayma'a et al., 2012; Tironi et al., 2012). Calcining raw clays at temperatures between 600-800°C leads to the formation of an active metastable state with high pozzolanic activity (Fernandez et al., 2011). The pozzolanic reaction of calcined clays and calcium hydroxide during cement hydration results in the formation of more binding phases, reducing the pore space in the cement paste (Davis, 1950; Massazza, 2002; Sabir et al., 2001). This can also lead to improved compressive strength development. The optimum calcination temperature to reach maximum pozzolanic activity depends on the mineralogy of the clays (He et al., 1994, 1996; He et al., 1995). A complete removal of hydroxyl groups upon calcination results in a collapsed and disarranged metastable structure with low crystallinity (Jeans and Bergaya, 2008; Sabir et al., 2001). In a comparative study of calcined illite, montmorillonite and kaolinite using X-Ray diffraction (XRD) and nuclear magnetic resonance spectroscopy (Al NMR), it could be shown that kaolinite undergoes the most significant structural changes upon calcination (Fernandez et al., 2011). Raw clays are often polymineral materials making it

difficult to find the optimum calcination temperature. If raw clays are heated at too high temperatures (> 900°C) recrystallization can take place, resulting in a decreased reactivity.

Ternary blends of cement, metakaolin and limestone have been investigated by many authors (Antoni et al., 2012; Avet and Scrivener, 2018a, b; Bishnoi and Maity, 2018; Cancio Díaz et al., 2017; Favier et al., 2018; Kunther et al., 2015; Nied et al., 2015; Scrivener et al., 2017; Tironi et al., 2015). However, the role of calcium carbonate in raw clays (before calcination) without kaolinite has been paid little attention to. The present authors have previously published extensive studies (Danner et al., 2015; Danner et al., 2012b, 2013; Justnes et al., 2011; Østnor et al., 2015) of what was called calcined "marl" for simplicity, but actually should be categorized as "calcareous mudstone" being a montmorillonite containing 25% calcium carbonate. It was shown that replacing cement with up to 50% “calcined marl” can lead to higher or equal 28 day compressive strength in mortars.

In this paper, the pozzolanic reactivity of a kaolin is compared to a calcareous montmorillonite. To explain the pozzolanic reactivity, structural changes upon heating were investigated by Fourier transformed infrared spectroscopy (FTIR), nuclear magnetic resonance spectroscopy (Al-NNR) and Mössbauer spectroscopy. Phase changes and microstructural changes were documented by X-ray diffraction (XRD) and scanning electron microscopy (SEM). Additionally, changes in specific surface area (BET), and ion release in an approximated concrete pore water was investigated by inductively coupled plasma mass spectrometry (ICP-MS).

2. Materials

Table 1 shows the phase composition of the Clay A and B and Table 2 shows the chemical composition of Clay A and B calcined at 800°C. The main mineral phases of Clay A are kaolinite, quartz and orthoclase. Clay B contains high amounts of montmorillonite and 25%

calcite. Clay B is a tertiary sediment and was deposited between the middle and late Eocene in a marine depositional environment (Grønbech et al., 2010). The calcite content derives to a large portion from coccoliths (Okkels and Juul, 2008). Pyrite was detected in Clay B, however, the chemical composition showed no SO_3. Under the SEM the pyrite distribution appeared only very localised in form of pyrite framboids (Figure 10). The non-homogeneous distribution of pyrite in Clay B might be a reason why SO_3 was not detected with XRF in the analysed sample. The cement used in mortar tests was Norcem Standard (CEM I 42.5 R) and the chemical composition is given in Table 2.

For ICP-MS investigations, an alkaline solution of pH 13.2 and a KOH:NaOH ratio of 2:1 was prepared. The alkaline solution is an approximated pore water based on analyses from the water of fresh paste from CEM I used in Norway. KOH and NaOH was chosen to achieve a pH value > 13, representative for concrete pore solution (Moreno et al., 2004; Williamson and Isgor, 2016).

3. Methods

3.1. Production of calcined clays

The thermal treatment of Clay A and B was executed at IBU-tec advanced materials AG (Weimar, Germany), using a direct natural gas heated rotary kiln. The kiln is designed for a continuous thermal treatment and was used to simulate trials under industrial conditions. The feed rate was 30 kg/h and the residence time in the kiln was 45 min. Clay A was calcined between 700-800°C as the highest pozzolanic reactivity of calcined kaolinite can be expected in this temperature range. Clay B was calcined at temperatures between 700-1000°C in steps of 50°C, as the temperature range of highest pozzolanic reactivity was unknown. The milling of the calcined clay lumps produced at IBU-tec was performed at UVR-FIA GmbH (Freiberg, Germany). The material was pre-crushed in a laboratory hammer mill equipped with a 1.6 mm

grid applying a circumferential speed of 33 m/s, to obtain a material with d_{95} = 1 mm. The finish grinding to a d_{50} < 10 µm (determined with laser granulometry) was performed with a discontinuous drum mill.

3.2. Quantitative mineralogical analysis of the raw clays by X-ray diffraction (XRD)

Bulk mineralogy of Clay A and B was performed on dried and ground samples using the back-loading technique. Followed by that, the ≤ 2 µm fraction (clay fraction) was separated from the bulk sample by means of sedimentation. The ≤ 2 µm fraction was smeared on a glass plate and dried in air. The clay fraction was investigated under three different conditions (a-c); a: untreated, b: after treatment with ethylene glycol vapours in a desiccator for 24 h at 60°C, c: after heating at 500°C for 1 h. For analysis, a PAN Analytical X'Pert Pro MPD equipped with a X'Celerator RTMS detector, an automatic divergence slit and a Cu-K<alpha> X-ray source was used. The samples were measured from 2-65° 2θ using a step size of 0.0170° 2θ and a step time of 20 sec. Data was collected at 45 kV and 40 mA. More details on the procedure of quantitative mineralogical analysis can be found in (Nielsen, 1994; Nielsen et al., 1989).

3.3. X-ray Fluorescence analysis (XRF*)*

XRF analysis was performed with a Bruker AXS S8 Tiger WDXRF equipped with a 4 kW generator. Dried and powdered clay samples were ignited at 850°C. Then 0.5 g of the dried clay sample was added to 5.0 g of a 2:1 mix of lithium- tetraborate and metaborate and 60 µg of lithium iodide. The mixture was fused in a Pt crucible and moulded to a glass disk.

3.4. Compressive strength of mortars

Mortars were prepared by substituting Portland cement (PC) with 20% calcined Clay A and B. The mixing procedure was according to the Norwegian Standard NS-EN 196-1 (2005). The

water to binder ratio (w/b) was held constant at 0.5 in all mortar mixes. In mortars with calcined Clay A and B, this was achieved by adding superplasticizer (Dynamon SP 130, Rescon Mapei) with about 0.3% by dry weight of mortar. The consistency of fresh mortar was determined using a flow table and the flow was within ± 5% of the reference mortar. The mortar mixes were cast in three 40x40x160 mm molds and stored in a cabinet for 24 hours at 23 ± 2°C and 90% relative humidity (RH). After 24 hours, the mortar prisms were removed from the molds and stored in saturated CH water to avoid leaching, for 28 days. After 28 days storage, the compressive strength was determined according to the Norwegian Standard NS-EN 196-1.

3.5. Specific surface area (BET)

BET specific surface area was measured with a Tristar 3000 Surface Area & Porosity Analyzer apparatus from Micromeritics. Prior to analysis the samples were degassed with a SmartPrep degasser (VacPrep 061) to remove adsorbed contaminants from the surface and pores of the samples.

3.6. X-ray Powder diffraction (XRD)

Powders of calcined Clay A and B were prepared for XRD measurements using the front loading technique. The samples were measured with a D8 Focus diffractometer from Bruker equipped with a Lynx Eye detector and a Cu-K<alpha> X-ray source. A fixed divergence slit of 0.2 mm was used. Measurements were taken from 5-65° 2θ with a step size of 0.2° 2θ and a step time of 1 sec. Data was collected at 40 kV and 30 mA.

3.7. Fourier transformed infrared spectroscopy (FT-IR)

FT-IR spectra were taken in the transmittance mode in the middle-IR (MIR) region. Samples of 2 mg were dispersed in 200 mg of KBr and pressed to pellets of 13 mm diameter using a

mechanical hand press. Measurements were performed using a Bruker IFS 66v FTIR spectrometer equipped with an IR source, KBr beam splitter, and DTGS KBr detector. For each sample, 200 scans in the 400 – 4000 cm-1 (MIR) spectral range were recorded with a resolution of 2 cm-1. A spectrum of the atmosphere was recorded for background corrections of the samples.

3.8. Nuclear magnetic resonance spectroscopy (^{27}Al-MAS-NMR)

The ^{27}Al MAS-NMR spectra have been recorded at 14.1 T, using a 4 mm CP/MAS NMR probe, a spinning speed of νR = 13.0 kHz, a 0.5 µs excitation pulse (~ 11° pulse) (Garg and Skibsted, 2016), a 2 s relaxation delay, ^{1}H decoupling during acquisition, and in between 6560 and 50300 scans.

3.9. Mössbauer spectroscopy

The Mössbauer measurements were carried out at room temperature on a spectrometer with a constant acceleration type of vibrator and a 57Co/Rh source. The samples were ground, mixed with BN (boron nitride) and spread out to form absorbers. Calibration spectra were recorded using natural iron foil at room temperature as a reference absorber. Spectra obtained were folded and analysed using the least-squares Mössbauer fitting program Recoil.

3.10. Electron probe micro analysis (EPMA)

All samples were cast in epoxy resin, plane polished in iso-propanol and coated with carbon. For analyses, a JEOL JXA-8500F EPMA equipped with 5 wavelength dispersive X-ray spectrometers (WDS) and an energy dispersive X-ray spectrometer (EDS) was used. All samples were investigated in the backscattered electron imaging (BEI) mode with an

accelerating voltage of 15 kV. All results from WDX measurements are given in atomic percent (at%).

3.11. Inductively coupled plasma mass spectrometry (ICP-MS)

Dispersions of Clay A and B and alkaline solution were prepared in a ratio of 1:30. 3 g of clay were added to 90 mL solution and constantly rotated in a plastic bottle for 3 days. After 3 days the plastic bottle was standing still to enable the clay to settle down on the bottom of the bottle. About 15 mL of the clear solution were taken off with a pipette for ICP-MS analysis. The same was done with a reference sample, composed of only alkaline solution. HR-ICP-MS analysis was performed using a Thermo Finnigan model Element 2 instrument. The samples were introduced using a SC-Fast autosampler with a peristaltic pump. The instrument was equipped with a concentric PFA-ST nebulizer connected to a Scott PFA spray chamber, aluminium sample and skimmer cones, a demountable torch and a quartz injector.

4. Results and discussion

4.1. Compressive strength of mortars

Figure 1 shows the 28 day compressive strength of mortars with 20% replacement of cement by calcined Clay A (left) and calcined Clay B (right). The black line is showing the compressive strength of the reference mortar without cement replacement. The compressive strength of the reference mortar was about 55 MPa. Clay A seemed to be very reactive within the calcination temperature range between 700-800°C. Within the whole temperature range, 20% replacement of cement with calcined Clay A resulted in compressive strength up to about 8 MPa higher than what was achieved with the reference mortar. Calcined Clay B showed a narrower reactivity window. The reactivity with regard to compressive strength development increased from 700-800°C followed by a decrease from 800-1000°C. 20% replacement of cement by Clay B

calcined at 800°C resulted in 7 MPa higher 28 day compressive strength compared to the reference mortar. Higher replacement levels of cement up to 50% were tested for Clay A and B at a calcination temperature of 800°C (Danner et al., 2015; Danner et al., 2012a; Danner et al., 2013). It could be shown that even with 50% cement replacement, higher or equal 28 day compressive strength was achieved compared to the reference mortar.

4.2. BET specific surface area

Table 3 shows the measured BET surface area of Clay A and B, raw, and calcined at 700 and 800°C. While the BET specific surface area of the montmorillonite rich Clay B decreased with increasing temperature, the kaolinite rich Clay A showed no change. When calcined to 700°C the specific surface of Clay B fell from 71.3 to 54.1 m^2/g. This is a result of a first collapse of the montmorillonite layers through dehydration of the interlayer spaces reducing the d-spacing of the mineral structure. This was confirmed with XRD presented in section 4.3. Upon further heating to 800°C, the specific surface dropped significantly to 15.1 m^2/g. The complete dehydroxylation caused a further decrease of the inner surfaces. Recrystallization was not observed with XRD for Clay B at 800°C. The specific surface of Clay A did not change from 100 to 800°C within the error of the measurement. Quartz and orthoclase do not undergo any significant changes when heated to these temperatures. Even the transformation of kaolinite to metakaolinite has only a minor impact on the specific surface (Fernandez et al., 2011; He et al., 1995).

XRD

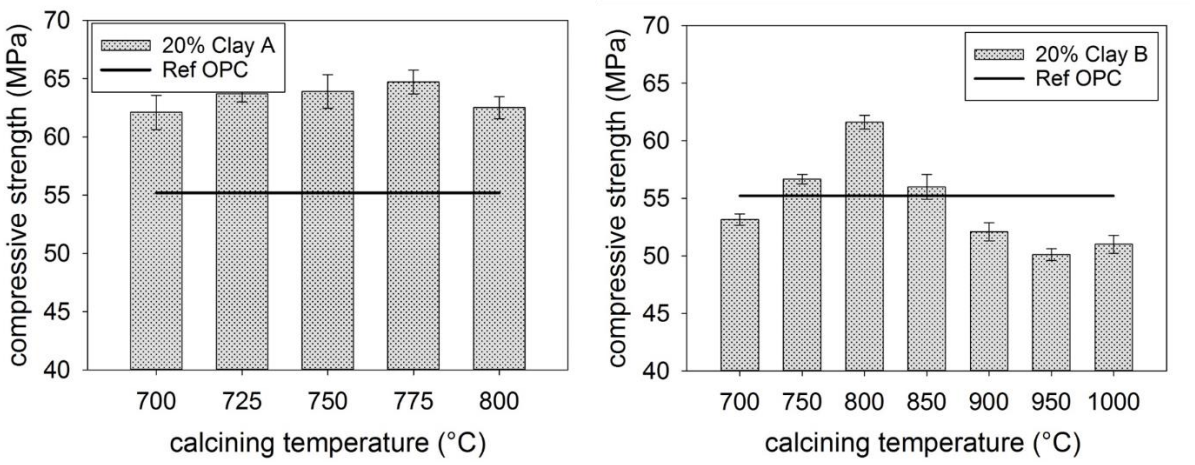

232

233 ***Figure 1: 28 day Compressive strength of mortars with 20% replacement of cement by calcined Clay A (left) and calcined***
234 ***Clay B (right).***

235

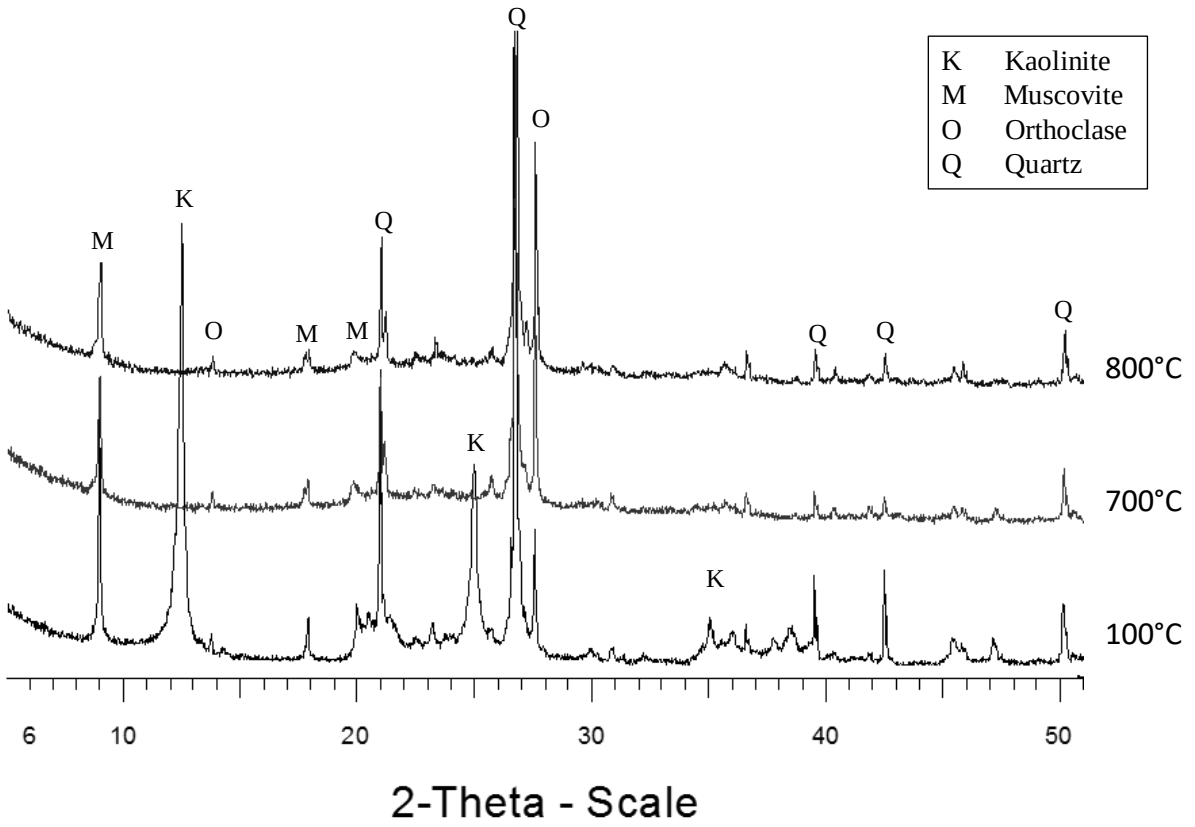

236

237 Figure 2 shows the XRD diffractograms of Clay A, raw and calcined at 700 and 800°C. When
238 calcined at 700°C, the kaolinite reflections disappeared due to dehydroxylation of the kaolinite
239 structure, i.e transformation of kaolinite to X-ray amorphous metakaolinite. This is visible in
240 the increased background of the diffractograms from Clay A calcined at 700 and 800°C. Quartz
241 and orthoclase minerals were not affected by the heat treatment. Muscovite reflections were

still visible at a calcination temperature of 800°C. The dihydroxylation of muscovite takes place between 850°C and 900°C (2003; Meyers and Speyer, 2003). The phase assemblage as visible in the XRD diffractograms did not change between 700-800°C. There is no recrystallization to expect in kaolin when burned at such relatively low temperatures. At temperatures above 1100°C, the formation of mullite may occur (Mota et al., 2009; Sperinck et al., 2011). The good pozzolanic reactivity of Clay A calcined at 700 and 800°C in mortar tests is coherent with the identical XRD diffractograms at 700 and 800°C. Already at 700°C, the transformation to metakaolin is complete and the pozzolanic reactivity does not increase further.

In Figure 3, the phase changes during the calcination of Clay B between 700-1000°C are presented. Raw Clay B was dried at 100°C so that the interlayer space of montmorillonite decreased due to dehydration. This caused a shift of the 001 montmorillonite reflection from about 6° 2θ to 9° 2θ resulting in an overlapping with the illite reflection at 8.9° 2θ. At a calcination temperature of 700°C the kaolinite reflection at 12.4° 2θ disappeared due to transformation to metakaolinite. Calcite was not completely decomposed until 850°C. Montmorillonite was visible until 800°C. It appeared from the background of the diffractograms that the highest amount of amorphous phases was present between 800-850°C. The main phases detected at temperatures above 850°C were anorthite ($CaAl_2Si_2O_8$), wollastonite ($CaSiO_3$) and diopside ($CaMgSi_2O_6$). Gehlenite ($Ca_2Al_2SiO_7$) appeared as an intermediate phase at 850 and 900°C. When coexisting with quartz or other SiO_2 minerals, gehlenite becomes unstable and reacts further to anorthite and wollastonite (Duminuco et al., 1998; Rathossi et al., 2004; Trindade et al., 2009). With regard to the compressive strength results obtained in the mortar tests, the beginning recrystallization of new stable and unreactive phases at 850°C explains the decreasing reactivity of Clay B at temperatures above that and hence the decrease in compressive strength of the mortars.

4.3. FT-IR spectroscopy

The FT-IR spectra of the raw and calcined Clay A are shown in Figure 4. Kaolinite showed four OH stretching bands at 3696, 3670, 3670, 3620 cm-1 (Chakchouk et al., 2009; Madejova and Komadel, 2001; Tironi et al., 2012). Additionally, three well-resolved Si-O stretching bands at 1114, 1032, 1008 cm-1, typical for kaolinite were observed. The absorption band at 696 cm-1 was assigned to Si-O stretching of kaolinite or quartz. The absorption band observed at 912 cm-1, is related to the Al-O-H deformation band of the octahedral sheet in the structure. Absorption bands observed at 538 and 469 cm-1 are attributed to Al-O-Si and Si-O-Si deformation bands respectively. The first describing the connection of octahedral and tetrahedral sheet in the kaolinite structure and the second reflecting the bonding of tetrahedra in the tetrahedral sheet. These signals were also visible in Clay B (Figure 5). Quartz and orthoclase was detected in the absorption bands at 795 and 755 cm-1 respectively.

Calcination at 700°C resulted in the disappearing of the OH stretching bands between 3600-3700 cm-1 and the Al-O-H deformation band at 912 cm-1. This indicates complete dehydroxylation of kaolinite. All samples appeared to adsorb water from the atmosphere visible in the bands at 3400 cm-1 and 1635 cm-1. The well-resolved Si-O stretching bands transformed into one wide peak with a maximum at about 1080 cm-1 upon calcination. This was explained with the formation of a 3 dimensional amorphous silica network (Madejová, 2003). The disappearing of the Al-O-Si deformation band at 538 cm-1 and the shifting of the Si-O-Si deformation band at 469 to a higher wavenumber has been observed by several authors (Madejová, 2003; Tironi et al., 2012). Additionally, new absorption bands appeared at 570 and 870 cm-1. These can most likely be ascribed to the amorphous metakaolinite structure. Especially the disappearance of the Al-O-Si deformation band and the shift and broadening in the Si-O-Si deformation band potentially imply significant structural changes in the local

292 environment of the Al and Si atoms in the octahedral and tetrahedral sheet. Increasing the
293 calcination temperature from 700 to 800°C did not result in a change of the FT-IR spectra. The
294 higher intensities of most of bands at a calcination temperature of 800°C, are explained by a
295 potential higher sample saturation in the KBr disk.
296 Figure 5 shows the FT-IR spectra of the raw and calcined Clay B. The band observed at 3620
297 cm-1 is typical for dioctahedral montmorillonites with a high amount of aluminium in the
298 octahedra (Madejová, 2003). The absorption band at 3699 cm-1 reflects the presence of
299 kaolinite. The OH stretching band of H_2O molecules at 3439 cm-1 is found in almost all clay
300 minerals, especially when smectite is dominating. Common for all smectites is the broad
301 complex Si-O stretching band at 1030 cm-1 (Madejová, 2003). Within this broad band a
302 shoulder was observed at around 1100 cm-1 which can be assigned to kaolinite. The Al-O-H
303 deformation band observed at 911 cm-1 is typical for dioctahedral smectite minerals
304 (Madejová, 2003). Calcium carbonate absorption bands were found at 713, 874, 1428 and 2514
305 cm-1. The absorption band at 1799 cm-1 is typical for several carbonate minerals and could
306 potentially be due to the small amounts of siderite found in Clay B (Table 1). The presence of
307 quartz was visible in the Si-O stretching bands at 796 cm-1 and 696 cm-1. Small amounts of
308 organic material showed bands at 2877 cm-1 and many smaller peaks at higher frequencies.
309 When calcined at 700°C the OH stretching band of kaolinite at 3699 cm-1 disappeared while
310 the OH stretching band of the montmorillonite at 3621 cm-1 was still visible. At 800°C
311 montmorillonite became dehydroxylated as well, also visible by the disappearing of the Al-O-
312 H deformation band at 911 cm-1. With increasing calcination temperature, the Si-O stretching
313 bands around 1030 cm-1 broadened indicating the presence of amorphous silica (Madejová,
314 2003). Potential distortion in the montmorillonite layers and modified bonding of the bridging
315 oxygen atoms was visible in the diminishing intensities of the Al-O-Si and Si-O-Si deformation
316 bands at 534 and 469 cm-1. The Si-O-Si band broadened, decreased in intensity and shifted to

higher frequencies. This confirms a lower crystallinity in the tetrahedral sheet and distortions in the arrangement of the tetrahedra. The completely disappearing Al-O-Si deformation band might reflect a decreasing content of octahedral cations (Madejová, 2003). The disappearance of the band at 534 cm-1 and the displacement of Si-O-Si band at 469 cm-1 was confirmed for kaolinite to metakaolinite transformation in several papers as a sign for the presence of an amorphous reactive phase (Chakchouk et al., 2009; Tironi et al., 2012). Calcium carbonate was not completely decomposed at 800°C confirming results from XRD. The partly decomposition of calcite was reflected in a peak broadening and a decreasing intensity of the band at 1428 cm-1. The higher intensities of some absorption bands in the sample calcined at 700°C are explained by a potential higher sample saturation in the KBr disk.

4.4. ^{27}Al MAS NMR

Figure 6 shows the ^{27}Al MAS NMR spectra of the raw and calcined Clay A. Spinning side bands are marked with asterisks. The chemical shifts at 71.4 ppm and 56.9 ppm originate from Al in tetrahedral coordination, and are typical for Al sites in layered clay mineral structures (70.8 ppm) and fully condensed $Al(OSi)_4$ sites (59.3 ppm) (Brown et al., 1987b; Drachman et al., 1997; Fernandez et al., 2011; Jeans and Bergaya, 2008; Skibsted, 2011). Al in tetrahedral coordination might represent the substitution of Al for Si in the tetrahedral sheet of muscovite. However, orthoclase present in Clay A also contains Al entirely in tetrahedral coordination and exhibits a chemical shift in the same region between 56-60 ppm (Zhou et al., 1997). The most intense chemical shift observed at 4.9 ppm reflects Al in octahedral coordination, i.e. octahedral sheets in kaolinite. The relative intensities were 2.6% (71.4 ppm), 11.9% (56.9 ppm) and 85.5% (4.9 ppm), confirming that most of the aluminium was present in octahedral sheets of the kaolinite structure.

The ^{27}Al MAS NMR spectrum of Clay A calcined at 800°C showed chemical shifts for Al in tetrahedral (57.2 ppm), five-fold (29 ppm) and octahedral (4.2 ppm) coordination (Fernandez et al., 2011; Rocha and Klinowski, 1990). An estimation of the relative intensities for the different sites, by spectral integration, gave relative intensities of 37.3% (57.2 ppm), 40.3% (29 ppm), and 22.4% (4.2 ppm). This indicates that Al was mainly present in 4 and 5-fold coordination in Clay A, calcined at 800°C. 4-fold coordinated Al was observed before in calcined kaolinite (Fernandez et al., 2011) but it cannot be excluded that a significant amount of the intensity of this peak derives from the orthoclase. The change in coordination and especially the presence of 5-coordinated Al clearly indicates a disordering and loss of crystallinity of the structure.

^{27}Al MAS NMR spectra of the raw and calcined Clay B (800°C) are shown in Figure 7. The spectrum of the raw Clay B showed three chemical shifts at 70.8 ppm, 59.3 ppm, and 4.3 ppm with the following relative intensities 5.4%, 16.0%, and 78.7%, respectively. As expected, Al was mainly present in the octahedral sheet of the montmorillonite. The spinning sidebands closest to the central-transition region are marked by asterisks.

The ^{27}Al NMR spectrum of Clay B calcined at 800°C showed two chemical shifts at 59.6 ppm and 3.7 ppm with the relative centre-band intensities of 95.1% and 4.9%, respectively. Octahedral Al in the raw montmorillonite has been almost completely converted to Al in tetrahedral coordination. The signal at 3.7 ppm in the calcined sample might represent residual octahedrally coordinated aluminium from montmorillonite (Drachman et al., 1997) or from kaolinite and illite (Fernandez et al., 2011). The dehydroxylation accompanied with the change in coordination for Al must result in significant structural alterations. The reorganizing octahedral sheet will induce distortions in the tetrahedral silicon sheet as well, from changing bond lengths and angles up to a complete separation (Drachman et al., 1997). This was

365 confirmed with FT-IR spectroscopy where a disappearing Al-O-Si band was observed upon
366 calcination.
367
368 **4.5. Mössbauer spectroscopy**
369 Mössbauer spectroscopy was only used to study Clay B. The iron content of Clay A was too
370 low to be studied by this method. Representative Mössbauer spectra of the raw and calcined
371 Clay B are shown in Figure 8. Data points and fitting are marked with crosses and black lines,
372 respectively. The individual red and blue lines correspond to the absorption of the Fe^{2+} and
373 Fe^{3+} components, respectively. The lines marked black in Figure 8a are the inner lines of the
374 six-line patterns emanating from the magnetic part. In the fitting procedure, both Fe^{2+} and Fe^{3+}
375 are represented by two absorption lines with equal intensities (doublets). The isomer shift (δ)
376 taken as the centre of the doublet, is referred to α-Fe as standard absorber. The electric
377 quadrupole splitting (Δ), is the splitting of the doublet. In the fitting, the isomer shift,
378 quadrupole splitting, doublet intensity (I) and the line width (Γ) were kept as varying
379 parameters. Both spectra showed strong resonances at around 0 - 2 mm/s as it is typical for clay
380 minerals (Murad and Wagner, 1998). The calcined Clay B showed furthermore resonances at
381 higher velocities (Figure 8b). These resonances are parts of six-line patterns originating from
382 a magnetic part of the sample. These outer lines representing the magnetic phases are rather
383 symmetric. The isomer shift (δ) was 0.36 (1) mm/s and the quadrupole coupling constant (ε)
384 was about - 0.11 (3) mm/s. The high fields are representative for hematite (α-Fe_2O_3). The field
385 distribution potentially derives from solid solutions of corundum-hematite (α-$Fe_{2-x}Al_xO_3$)
386 (Brown et al., 1987a; Majzlan et al., 2002). The substitution of Fe with Al would result in a
387 lowering of the field. With this interpretation, the whole magnetic signal comes from Fe^{3+}. The
388 intensities of these magnetic patterns showed, within error, 30 mass% of Fe in the calcined
389 sample to be present in the magnetic part.

390 The analysis of spectra, recorded with lower velocity scale, (Figure 8a) were performed with
391 varying number of quadrupole split doublets. The spectrum of the raw montmorillonite
392 consisted mainly of a slightly split doublet and wider doublets (marked blue in the figure).
393 From the fitting of the doublets in the raw montmorillonite, Fe^{3+} and Fe^{2+} were detected. In
394 Table 4 averaged hyperfine interaction values for the ferric and ferrous patterns of raw and
395 calcined Clay B are given. The isomer shifts and quadrupole splitting's found are characteristic
396 for clay minerals, like kaolinite, illite and montmorillonite (Murad and Cashion, 2011). The
397 values for the isomer shift of Fe^{3+} and Fe^{2+} indicated octahedral coordination for both (Takeda
398 et al., 1979). Fe^{3+} and Fe^{2+} were thus substituted for Al^{3+} and Mg^{2+} in the octahedral layer of
399 montmorillonite. All changes recorded for the iron species are therefore representative for any
400 change in the octahedral layer of the structure, i.e. the Al environment. The allowed quadrupole
401 splitting versus isomer shift combinations for ^{57}Fe were investigated in (Murad and Cashion,
402 2011). Different combinations result in different coordination for Fe^{3+} and Fe^{2+}. The
403 coordination of Fe^{3+} seemed to change towards 5 and 6 upon calcination as the quadrupole
404 splitting increased. Increasing quadrupole splitting may also be due to changes in the ligand
405 structure for Fe caused by dehydroxylation. The isomer shift of Fe^{2+} decreased from the raw to
406 the calcined Clay B and so did the quadrupole splitting, indicating a change in coordination
407 towards 4. The values obtained for isomer shift and quadrupole splitting are in agreement with
408 literature and were interpreted as the result of strong distortions in the octahedral layer of
409 calcined clay mineral structures (MacKenzie and Rogers, 1977; Takeda et al., 1979).
410 During the calcination process the Fe^{2+} was expected to be oxidized mostly to Fe^{3+} at 800°C
411 since the calcination takes place in air. The relative amounts (I) of different Fe valences are
412 presented in Table 4 and show that almost all the iron was oxidized in the calcined Clay B.
413 Induced stresses and distortions leading to a highly disorganized calcined montmorillonite

structure due to the oxidation of iron accompanied with increasing quadrupole splitting values was partly confirmed by (Miller et al., 1963; Simopoulos et al., 1975; Tichit et al., 1988).

4.6. SEM

Figure 9a-b shows images of the raw Clay A. In the fine-grained kaolin matrix, larger grains of orthoclase and quartz were observed. Only small kaolinite crystallites with lamellar texture were found in the matrix. The presence of kaolinite was verified by WDX analysis. In contrast to that, large crystallites of muscovite with a size up to 50 µm were found (Figure 9b). When calcined at 700-800°C the kaolinite matrix showed only a slightly modified microstructure (Figure 9c-f). The kaolinites lamellar texture appeared to widen up upon calcination. In point 1 & 2 in Figure 9c-d, the element composition was analysed by WDS (wavelength dispersive spectra). The composition was similar in both points with about 20% Al and 20% Si (both in atomic percent). A composition with Al/Si ratio of 1/1 is typical for metakaolinite with the formula $Al_2Si_2O_5$. Figure 9e-f show two metakaolinite particles with a size of about 5 µm.

Clay B originates from marine sedimentation and contains calcareous microfossils. The calcium carbonate content in Clay B derives to a large extent from coccoliths, observed all over the raw Clay B (Figure 10a). Coccoliths are the exoskeletons of a group of plant plankton called coccolithophores which belong to the algal division Haptophyta (Young and Henriksen, 2003). Pyrite was found only locally in form of pyrite framboids (Figure 10b) (Lauf et al., 1982). Clay B calcined at 700°C is presented in Figure 10c-d. Coccoliths appeared still stable at this temperature. However, it appeared that the dense matrix widened up. When calcined at 800°C the morphology was altered significantly (Figure 10e-f). The coccoliths were decomposed leaving cavities in the montmorillonite matrix. At the same time the matrix appeared more vitreous (Figure 10e). Moreover, new larger glassy particles were found all over calcined Clay B (Figure 10f). The lower BET specific surface area measured in the calcined Clay B is most

likely the result of these new formed glassy phases. The formation of a liquid phase in calcite bearing clays has also been observed by other authors (Duminuco et al., 1998; Nodari et al., 2007; Trindade et al., 2009). The composition of this new formed phase was measured with WDS analysis. The average composition of 3 particles in atom% was 19% Si, 8% Al, 8% Fe, 5% Ca, 2% Mg, 2% Na+K and 55% O. The result obtained in atom% of the elements was recalculated in weight% of the respective oxides. The calculated oxide composition was similar to the chemical composition measured with XRF of the initial raw Clay B (Danner, 2013). However, the analysis was performed on a limited amount of particles and might not be representative for the whole calcined Clay B. The glassy phase potentially contributes to the good pozzolanic reactivity of the calcined Clay B shown in mortar tests.

4.7. Inductively coupled plasma mass spectroscopy (ICP-MS)

ICP-MS analysis was performed to investigate the release of ions from the raw and calcined Clay A and B in an approximated concrete pore water. Of particular interest was the release of silicon, aluminium and alkalis as these are the main elements contributing to the pozzolanic reaction. The results are given in Table 5. In the raw Clay A, the release of silicon and aluminium was about equal. This can be explained by the mineral structure of kaolinite, having the octahedral and tetrahedral sheet exposed equally. Due to that, the aluminium release of Clay A was considerably higher than for Clay B where montmorillonite dominates. In the layered structure of montmorillonite, the octahedral sheet is located between two tetrahedral sheets. When calcined at 800°C, both the release of silicon and aluminium increased considerably. Calcined Clay A released higher amounts of silicon and aluminium than Clay B, indicating higher pozzolanic reactivity in cementitious binders. In the raw Clay B, the release of silicon was higher than the release of aluminium. As explained above, the tetrahedral sheets of montmorillonite are more exposed to the alkaline solution while the octahedral sheet is

shielded between the tetrahedral sheets. When calcined at 800°C the release of silicon decreased while the release of aluminium increased. This might be explained with structural rearrangement of the metastable structure. The release of calcium from Clay B increased upon calcination. Calcium release in Clay B derives probably from calcite and montmorillonite.

For potassium and sodium, negative values were measured. That means that higher amounts of potassium and sodium were measured in the pure reference solution (alkaline solution without Clay A or Clay B). Reason could be higher alkali ad- and absorption than what was released from Clay A and B. Especially potassium was reduced in much higher magnitude than sodium in the solution. The potassium ion with its ionic radius of about 1.38 Å fits perfectly in the cavity of the pseudo-hexagonal rings of oxygens of the adjacent silica tetrahedral sheet of illite or smectite minerals (Murray, 1999).

5. Conclusions

In this paper the potential use of two raw clays (Clay A: kaolin; Clay B: calcareous montmorillonite) as supplementary cementitious materials in blended cements is investigated. The pozzolanic reactivity of Clay A and B is explained by characterizing the structural changes upon calcination with XRD, , FT-IR, Al-NMR, Mössbauer spectroscopy, SEM and ICP-MS. The main conclusions are listed below.

- Compressive strength of mortars with 20% replacement of cement by calcined Clay A and B resulted in more than 10% strength increase after 28 day curing.
- At the temperature of highest pozzolanic reactivity (Clay A: 700-800°C; Clay B: 800°C) kaolinite and montmorillonite were completely dehydroxylated. However, the calcite in Clay B was not completely decomposed.

- FT-IR indicated changes in the connectivity of tetrahedral and octahedral sheets of the kaolinite and montmorillonite structure and showed the formation of 3-dimensional amorphous silica networks.
- In Clay A, most of the octahedral coordinated Al changed to 5-fold coordination upon calcination. In calcined Clay B, the coordination of Al was changed to tetrahedral coordination.
- Oxidation of iron during calcination resulted in strong distortions of the montmorillonite structure in Clay B. The coordination of Fe^{3+} was changing to 5-fold while the coordination of Fe^{2+} was changing towards 4-fold.
- Under the SEM, reactive metakaolinite particles were observed in Clay A. In Clay B, the formation of a glass phase due to reaction of coccoliths ($CaCO_3$) and montmorillonite was observed.
- When calcined at 800°C, Clay A and B showed increased release of Al in concrete pore water. Clay A did also show increased release of Si. This contributes to the pozzolanic reaction forming more binding phases in cementitious systems.

Acknowledgements:

Saint-Gobain Weber is acknowledged for initiating and financing this research project. SINTEF Building and Infrastructure is acknowledged for the cooperation, support with mortar testing and discussing the results of this research. Prof. Jørgen Skibsted (University of Aarhus, Denmark) and Prof. Ole Bjørnslev Nielsen (University of Aarhus, Denmark) are acknowledged for performing NMR analysis and the mineralogical analysis of the raw clays, respectively. Lennart Häggström (University of Uppsala, Sweden) is acknowledged for performing Møssbauer analysis.

References

2003. Handbook of Thermal Analysis and Calorimetry, in: Brown, M.E., Gallagher, P.K. (Eds.), Handbook of Thermal Analysis and Calorimetry. Elsevier Science B.V., p. ii.

2005. Standard CEN - EN 196-1 Methods of testing cement Part1: Determination of strength. European Committee for Standardization.

Al-Rawas, A.A., Hago, A.W., Al-Lawati, D., Al-Battashi, A., 2001. The Omani artificial pozzolans (sarooj). Cement, concrete and aggregates 23, 19-26.

Alujas, A., Almenares, R.S., Betancourt, S., Leyva, C., 2015. Pozzolanic reactivity of low grade kaolinitic clays: influence of mineralogical composition, Calcined Clays for Sustainable Concrete. Springer, pp. 339-345.

Antoni, M., Rossen, J., Martirena, F., Scrivener, K., 2012. Cement substitution by a combination of metakaolin and limestone. Cement and Concrete Research 42, 1579-1589.

Aras, A., Albayrak, M., Arikan, M., Sobolev, K., 2007. Evaluation of selected kaolins as raw materials for the Turkish cement and concrete industry. Clay Minerals 42, 233-244.

Avet, F., Scrivener, K., 2018a. Hydration Study of Limestone Calcined Clay Cement (LC3) Using Various Grades of Calcined Kaolinitic Clays. Springer Netherlands, Dordrecht, pp. 35-40.

Avet, F., Scrivener, K., 2018b. Reaction Degree of Metakaolin in Limestone Calcined Clay Cement (LC3). Springer Netherlands, Dordrecht, pp. 41-45.

Berriel, S.S., Favier, A., Domínguez, E.R., Machado, I.S., Heierli, U., Scrivener, K., Hernández, F.M., Habert, G., 2016. Assessing the environmental and economic potential of Limestone Calcined Clay Cement in Cuba. Journal of Cleaner Production 124, 361-369.

Beuntner, N., Thienel, K.C., 2015. Properties of Calcined Lias Delta Clay—Technological Effects, Physical Characteristics and Reactivity in Cement. Springer Netherlands, Dordrecht, pp. 43-50.

Bishnoi, S., Maity, S., 2018. Limestone Calcined Clay Cement: The Experience in India This Far. Springer Netherlands, Dordrecht, pp. 64-68.

Brown, I.W., Mackenzie, K.J., Cardile, C., 1987a. Lattice parameters and Mössbauer spectra of iron-containing corundum (α-Al 2 O 3). Journal of materials science letters 6, 535-540.

Brown, I.W., MacKenzie, K.J., Meinhold, R., 1987b. The thermal reactions of montmorillonite studied by high-resolution solid-state29Si and27Al NMR. Journal of materials science 22, 3265-3275.

Cancio Díaz, Y., Sánchez Berriel, S., Heierli, U., Favier, A.R., Sánchez Machado, I.R., Scrivener, K.L., Martirena Hernández, J.F., Habert, G., 2017. Limestone calcined clay cement as a low-carbon solution to meet expanding cement demand in emerging economies. Development Engineering 2, 82-91.

Chakchouk, A., Samet, B., Mnif, T., 2006. Study on the potential use of Tunisian clays as pozzolanic material. Applied clay science 33, 79-88.

Chakchouk, A., Trifi, L., Samet, B., Bouaziz, S., 2009. Formulation of blended cement: Effect of process variables on clay pozzolanic activity. Construction and Building Materials 23, 1365-1373.

Damtoft, J.S., Lukasik, J., Herfort, D., Sorrentino, D., Gartner, E.M., 2008. Sustainable development and climate change initiatives. Cement and Concrete Research 38, 115-127.

Danner, T., 2013. Reactivity of calcined clays, Doctoral Thesis, 2013:218. Norwegian University of Science and Technology - NTNU, p. 229.

Danner, T., Justnes, H., Norden, G., Østnor, T.A., 2015. Feasibility of Calcined Marl as an Alternative Pozzolanic Material,, in: Scrivener, K., Favier, A. (Eds.), 1st International Conference on Calcined Clays for Sustainable Concrete. Rilem Bookseries, Lausanne.
Danner, T., Justnes, H., Ostnor, T., 2012a. Calcined marl as a pozzolan for sustainable development of the cement and concrete industry. ACI Special Publication 289.
Danner, T., Østnor, T.A., Justnes, H., 2012b. Calcined Marl as a Pozzolan for Sustainable Development of the Cement and Concrete Industry, 12th International Conference on recent Advances in Concrete Technology and Sustainability Issues. American Concrete Institute, Prague.
Danner, T., Østnor, T.A., Justnes, H., 2013. Thermally activated marl as a pozzolan for cementitious based products, Twin Covilha International Conference on Civil Engineering - Towards a better environment and The Concrete Future, Covilha, Portugal.
Davis, R.E., 1950. A review of pozzolanic materials and their use in concretes, Symposium on Use of Pozzolanic Materials in Mortars and Concretes. ASTM International.
Drachman, S., Roch, G., Smith, M.E., 1997. Solid state NMR characterisation of the thermal transformation of Fuller's Earth. Solid State Nuclear Magnetic Resonance 9, 257-267.
Duminuco, P., Messiga, B., Riccardi, M.P., 1998. Firing process of natural clays. Some microtextures and related phase compositions. Thermochimica Acta 321, 185-190.
Ernst Worrell, Lynn Price, Nathan Martin, Chris Hendriks, Meida, L.O., 2001. CARBON DIOXIDE EMISSIONS FROM THE GLOBAL CEMENT INDUSTRY. Annual Review of Energy and the Environment 26, 303-329.
Favier, A., Zunino, F., Katrantzis, I., Scrivener, K., 2018. The Effect of Limestone on the Performance of Ternary Blended Cement LC3: Limestone, Calcined Clays and Cement. Springer Netherlands, Dordrecht, pp. 170-175.
Fernandez, R., Martirena, F., Scrivener, K.L., 2011. The origin of the pozzolanic activity of calcined clay minerals: A comparison between kaolinite, illite and montmorillonite. Cement and Concrete Research 41, 113-122.
Garg, N., Skibsted, J., 2016. Pozzolanic reactivity of a calcined interstratified illite/smectite (70/30) clay. Cement and Concrete Research 79, 101-111.
Gartner, E., 2004. Industrially interesting approaches to “low-CO2” cements. Cement and Concrete Research 34, 1489-1498.
Grønbech, G.L., Nielsen, B.N., Ibsen, L.B., 2010. Comparison of plasticity index of Søvind marl found by use of Casagrande cup, fall cone apparatus and loss on ignition. Department of Civil Engineering, Aalborg University, DCE Technical Reports 87, 14.
He, C., Makovicky, E., Osbaeck, B., 1994. Thermal stability and pozzolanic activity of calcined kaolin. Applied Clay Science 9, 165-187.
He, C., Makovicky, E., Osbaeck, B., 1996. Thermal treatment and pozzolanic activity of Na- and Ca-montmorillonite. Applied Clay Science 10, 351-368.
He, C., Osbaeck, B., Makovicky, E., 1995. Pozzolanic reactions of six principal clay minerals: activation, reactivity assessments and technological effects. Cement and concrete research 25, 1691-1702.
Huenger, K.-J., Gerasch, R., Sander, I., Brigzinsky, M., 2018. On the Reactivity of Calcined Clays from Lower Lusatia for the Production of Durable Concrete Structures. Springer Netherlands, Dordrecht, pp. 205-211.
Jeans, C., Bergaya, G., 2008. Handbook of Clay Science. Geological Magazine 145, 444.
Justnes, H., Østnor, T., Danner, T., 2011. Calcined marl as effective pozzolana, Proceedings of the International RILEM Conference on Advances in Construction Materials Through Science and Engineering.
Kunther, W., Dai, Z., Skibsted, J., 2015. Thermodynamic Modeling of Portland Cement—Metakaolin—Limestone Blends. Springer Netherlands, Dordrecht, pp. 143-149.

608 Lauf, R.J., Harris, L.A., Rawlston, S.S., 1982. Pyrite framboids as the source of magnetite
609 spheres in fly ash. Environmental Science & Technology 16, 218-220.
610 MacKenzie, K., Rogers, D., 1977. Thermal and Mössbauer studies of iron-containing hydrous
611 silicates: I. nontronite. Thermochimica Acta 18, 177-196.
612 Madejová, J., 2003. FTIR techniques in clay mineral studies. Vibrational spectroscopy 31, 1-
613 10.
614 Madejova, J., Komadel, P., 2001. Baseline studies of the clay minerals society source clays:
615 infrared methods. Clays and clay minerals 49, 410-432.
616 Majzlan, J., Navrotsky, A., Evans, B.J., 2002. Thermodynamics and crystal chemistry of the
617 hematite–corundum solid solution and the FeAlO3 phase. Physics and Chemistry of Minerals
618 29, 515-526.
619 Massazza, F., 2002. Properties and applications of natural pozzolanas. Structure and
620 Performance of Cements, 326-352.
621 Mehta, P.K., 1999. Concrete Technology for Sustainable Development. Concrete International
622 21, 47-53.
623 Meyers, K.S., Speyer, R.F., 2003. Chapter 6 - Thermal Analysis of Clays, in: Brown, M.E.,
624 Gallagher, P.K. (Eds.), Handbook of Thermal Analysis and Calorimetry. Elsevier Science
625 B.V., pp. 261-306.
626 Miller, J.G., Haden, W.L., Oulton, T.D., 1963. Oxidizing power of the surface of attapulgite
627 clay, Clays & Clay Minerals. Citeseer.
628 Moreno, M., Morris, W., Alvarez, M.G., Duffó, G.S., 2004. Corrosion of reinforcing steel in
629 simulated concrete pore solutions: Effect of carbonation and chloride content. Corrosion
630 Science 46, 2681-2699.
631 Mota, L., Toledo, R., Faria Jr, R., da Silva, E., Vargas, H., Delgadillo-Holtfort, I., 2009.
632 Thermally treated soil clays as ceramic raw materials: characterization by X-ray diffraction,
633 photoacoustic spectroscopy and electron spin resonance. Applied Clay Science 43, 243-247.
634 Murad, E., Cashion, J., 2011. Mössbauer spectroscopy of environmental materials and their
635 industrial utilization. Springer Science & Business Media.
636 Murad, E., Wagner, U., 1998. Clays and clay minerals: the firing process. Hyperfine
637 interactions 117, 337-356.
638 Murray, H., 1999. Applied clay mineralogy today and tomorrow. Clay minerals 34, 39-39.
639 Nied, D., Stabler, C., Zajac, M., 2015. Assessing the Synergistic Effect of Limestone and
640 Metakaolin. Springer Netherlands, Dordrecht, pp. 245-251.
641 Nielsen, O.B., 1994. Lithostratigraphy and sedimentary petrography of the Paleocene and
642 Eocene sediments from the Harre borehole, Denmark. Aarhus Geoscience 1, 15-34.
643 Nielsen, O.B., Cremer, M., Stein, R., Thiébault, F., Zimmermann, H., 1989. 8. ANALYSIS
644 OF SEDIMENTARY FACIES, CLAY MINERALOGY, AND GEOCHEMISTRY OF
645 THE PALEOGENE SEDIMENTS OF SITE 647, LABRADOR SEA. Proceedings of the
646 Ocean Drilling Program, Scientific Results 105, 101-110.
647 Nodari, L., Marcuz, E., Maritan, L., Mazzoli, C., Russo, U., 2007. Hematite nucleation and
648 growth in the firing of carbonate-rich clay for pottery production. Journal of the European
649 Ceramic Society 27, 4665-4673.
650 Okkels, N., Juul, K., 2008. Søvindmergel. GEO Subsurface Expertise, Aarhus, Denmark.
651 Østnor, T., Justnes, H., Danner, T., 2015. Reactivity and Microstructure of Calcined Marl as
652 Supplementary Cementitious Material, Calcined Clays for Sustainable Concrete. Springer, pp.
653 237-244.
654 Rathossi, C., Tsolis-Katagas, P., Katagas, C., 2004. Technology and composition of Roman
655 pottery in northwestern Peloponnese, Greece. Applied Clay Science 24, 313-326.
656 Rocha, J., Klinowski, J., 1990. 29 Si and 27 Al magic-angle-spinning NMR studies of the
657 thermal transformation of kaolinite. Physics and Chemistry of Minerals 17, 179-186.

Sabir, B.B., Wild, S., Bai, J., 2001. Metakaolin and calcined clays as pozzolans for concrete: a review. Cement and Concrete Composites 23, 441-454.
Schneider, M., Romer, M., Tschudin, M., Bolio, H., 2011. Sustainable cement production—present and future. Cement and Concrete Research 41, 642-650.
Scrivener, K., Martirena, F., Bishnoi, S., Maity, S., 2017. Calcined clay limestone cements (LC3). Cement and Concrete Research.
Shayma'a, K.A., Malath, Q.A.-Q., Dalya Kh, A.-D., Firas, F.A.-H., Abdul Wahab, A.A.-A., 2012. EVALUATION OF Al-AMIJ AND AL-HUSSAINIYAT CLAYSTONES (IRAQI WESTERN DESERT) FOR THE PRODUCTION OF POZZOLANA. Iraqi Bulletin of Geology and Mining مجلة العراقية والتعدين الجيولوجيا 8, 1-15.
Simopoulos, A., Kostikas, A., Sigalas, I., Gangas, N., Moukarika, A., 1975. Mössbauer study of transformations induced in clay by firing. Clays and Clay Minerals 23, 393-399.
Skibsted, J., 2011. 27Al MAS NMR investigation of three clay samples. Aarhus University.
Sperinck, S., Raiteri, P., Marks, N., Wright, K., 2011. Dehydroxylation of kaolinite to metakaolin—a molecular dynamics study. Journal of Materials Chemistry 21, 2118-2125.
Takeda, M., Kawakami, O., Tominaga, T., 1979. 57Fe MÖSSBAUER SPECTROSCOPIC STUDIES OF STRUCTURAL CHANGES OF MONTMORILLONITE ON HEATING IN REDUCING ATMOSPHERE. Le Journal de Physique Colloques 40, C2-472-C472-474.
Tichit, D., Fajula, F., Figueras, F., Ducourant, B., Mascherpa, G., Gueguen, C., Bousquet, J., 1988. SINTERING OF MONTOMORILLONITES PILLARED BY HYDROXY-ALUMINIUM SPECIES. CLAYS CLAY MINER. Clays Clay Miner. 36, 369.
Tironi, A., Scian, A.N., Irassar, E.F., 2015. Ternary Blended Cement with Limestone Filler and Kaolinitic Calcined Clay. Springer Netherlands, Dordrecht, pp. 195-201.
Tironi, A., Trezza, M.A., Scian, A.N., Irassar, E.F., 2012. Kaolinitic calcined clays: Factors affecting its performance as pozzolans. Construction and Building Materials 28, 276-281.
Trindade, M., Dias, M., Coroado, J., Rocha, F., 2009. Mineralogical transformations of calcareous rich clays with firing: a comparative study between calcite and dolomite rich clays from Algarve, Portugal. Applied Clay Science 42, 345-355.
Williamson, J., Isgor, O.B., 2016. The effect of simulated concrete pore solution composition and chlorides on the electronic properties of passive films on carbon steel rebar. Corrosion Science 106, 82-95.
Young, J.R., Henriksen, K., 2003. Biomineralization within vesicles: the calcite of coccoliths. Reviews in mineralogy and geochemistry 54, 189-215.
Zhou, L., Guo, J., Yang, N., Li, L., 1997. Solid-state nuclear magnetic resonance and infrared spectroscopy of alkali feldspars. Science in China Series D: Earth Sciences 40, 159-165.

695 ***Table 1: Mineralogical composition of Clay A and B before calcination***

Phase (mass%)	**A**	**B**
Kaolinite	47	8
Montmorillonite	—	54
Illite		4
Muscovite	2	—
Quartz	18	4
Orthoclase	34	—
Calcite	—	25
Siderite	—	3
Pyrite	—	1

696

697 ***Table 2: Chemical composition of Clay A and B calcined at 800°C and the cement used in mortar tests***

Oxide (%)	**A**	**B**	**Cement**
SiO_2	60.6	48.7	19.9
Al_2O_3	30.0	17.8	4.8
Fe_2O_3	3.4	10.4	3.3
CaO	0.1	13.8	61.9
K_2O	3.2	2.4	1.0
Na_2O	—	0.7	0.5
MgO	0.4	2.8	2.7
MnO	0.0	0.2	
P_2O_5	0.10	0.2	0.2
TiO_2	0.4	1.0	
SO_3			3.3
Total	98.2	98.0	97.6
LOI	1.8	2.0	2.4

698

699 ***Table 3: BET specific surface area of raw and calcined Clay A and Clay B***

	BET Surface Area (m^2/g)		
Sample Name	raw	700°C	800°C
Clay A	18	20	19
Clay B	71	54	15

700

701 **Table 4: Mössbauer averaged results. Isomer shift δ, quadrupole splitting Δ and line width at half**
702 **maximum Γ are given in mm/s, while the intensities I are given in %. The errors in the parameters are: δ**
703 **(± 0.01 mm/s), Δ (± 0.05 mm/s), I (± 1%) and Γ (± 0.02 mm/s).**

	Fe^{3+}				**Fe^{2+}**			
Sample	**δ**	**Δ**	**I**	**Γ**	**δ**	**Δ**	**I**	**Γ**
raw Clay B	0.39	0.52	77	0.24	1.12	2.20	23	0.17
calcined Clay B	0.33	1.21	63	0.31	0.95	1.90	7	0.33

704

705

706

707 ***Table 5: Ion release from raw and calcined Clay A and B dissolved in approximated concrete pore water (0.132 M, pH =***
708 ***13.2, KOH/NaOH = 2/1)***

	Si 30 [mg/L]	**Al 27 [mg/L]**	**Ca 44 [mg/L]**	**Fe 56 [mg/L]**	**Na 23 [mg/L]**	**K 39 [mg/L]**	**P 31 [mg/L]**	**Cl 35 [mg/L]**
Clay A raw	41.9	43.9	1.0	0.0	-158.2	-1302	2.3	0.0
Clay A 800	106.2	154.1	0.0	0.2	-126.3	-798.3	6.0	0.0
Clay B raw	66.7	1.9	2.9	0.0	-13.0	-752.2	0.1	0.0
Clay B 800	20.9	29.4	15.7	0.0	-40.7	-165.5	0.0	0.0

709

710

711

712

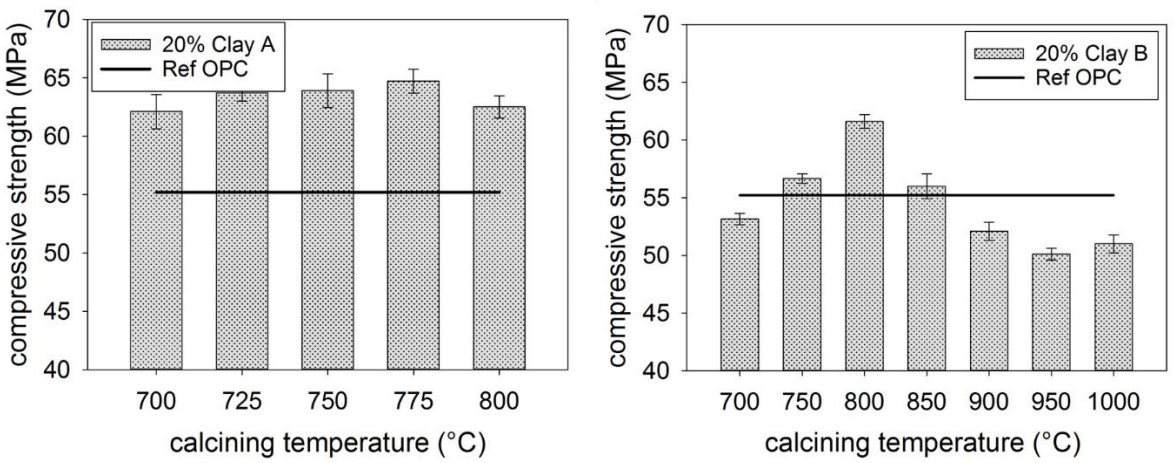

713

714 ***Figure 1: 28 day Compressive strength of mortars with 20% replacement of cement by calcined Clay A (left) and calcined***
715 ***Clay B (right).***

716

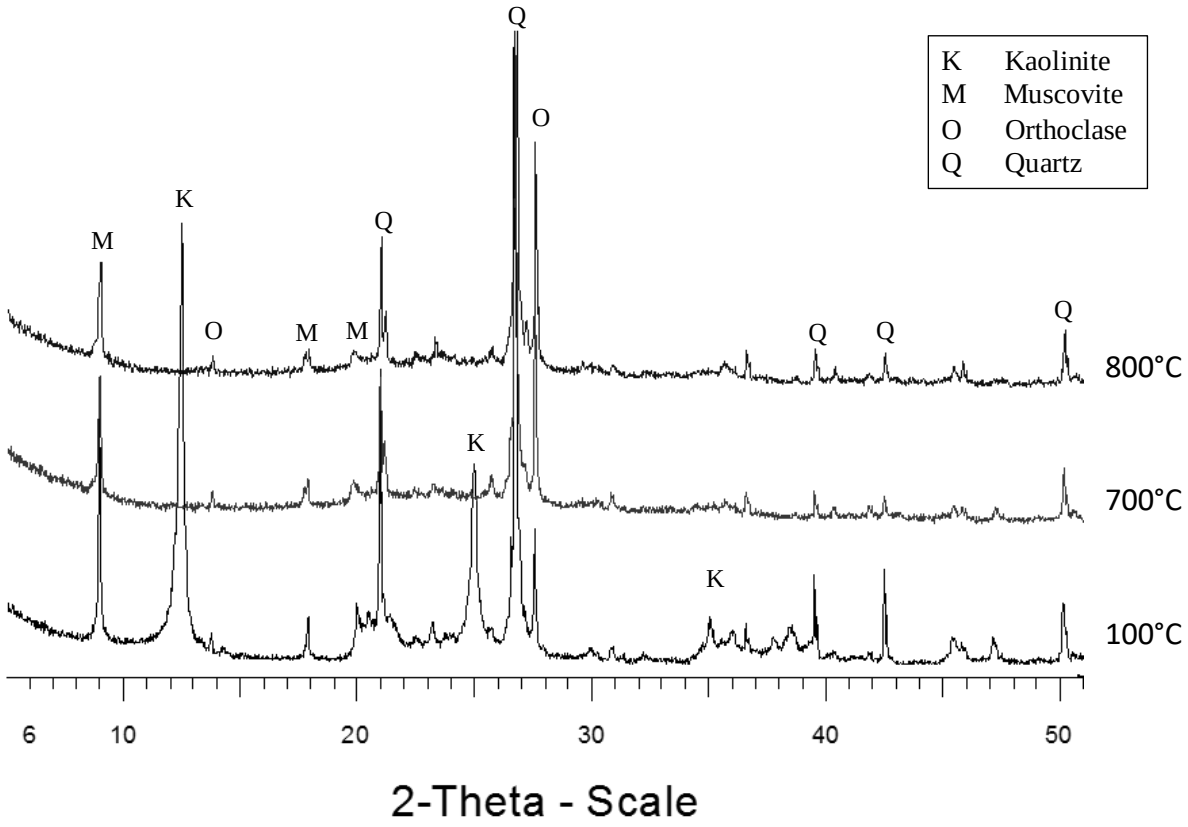

717

718 ***Figure 2: XRD diffractogram of raw and calcined Clay A***

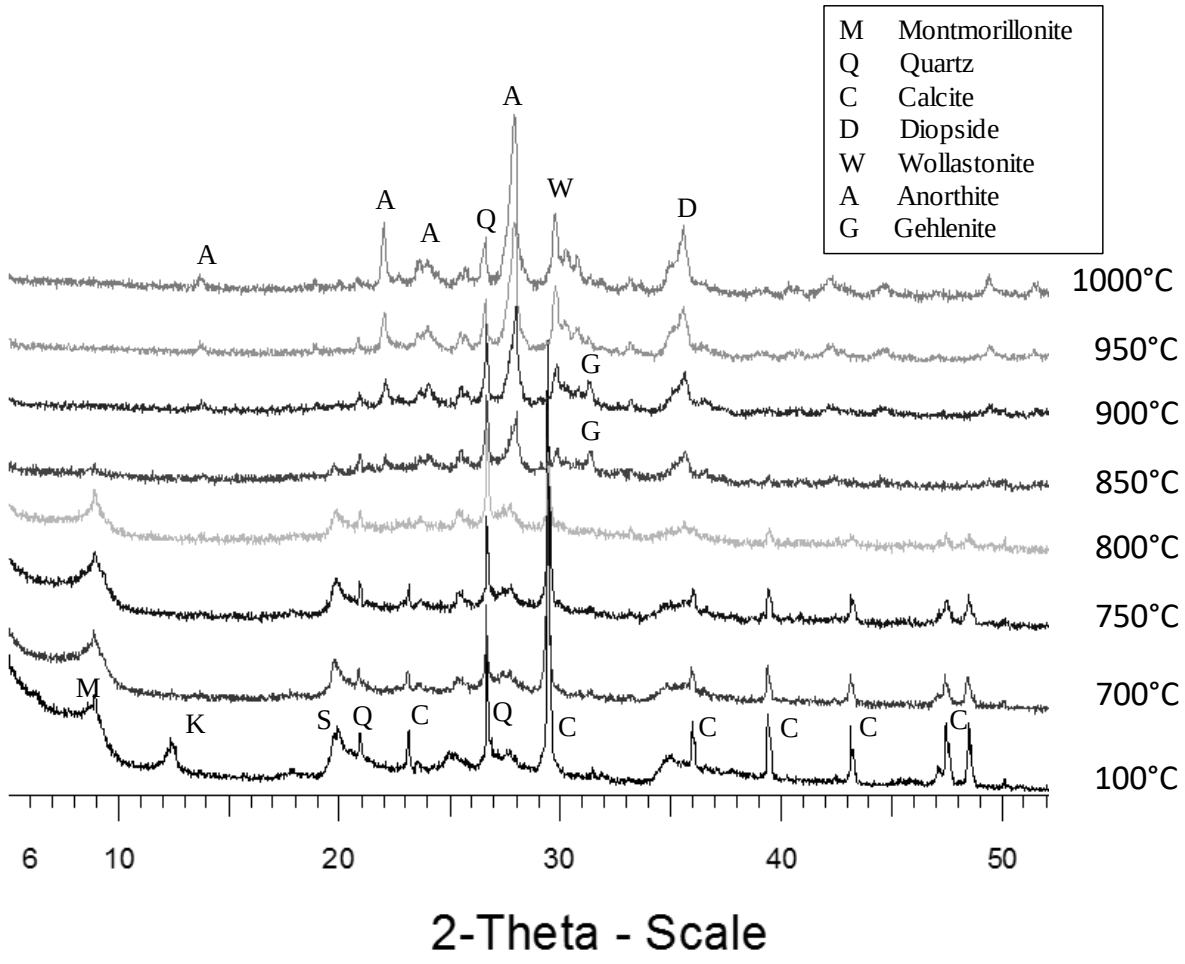

719

720 ***Figure 3: XRD diffractogram of raw and calcined Clay B***

721

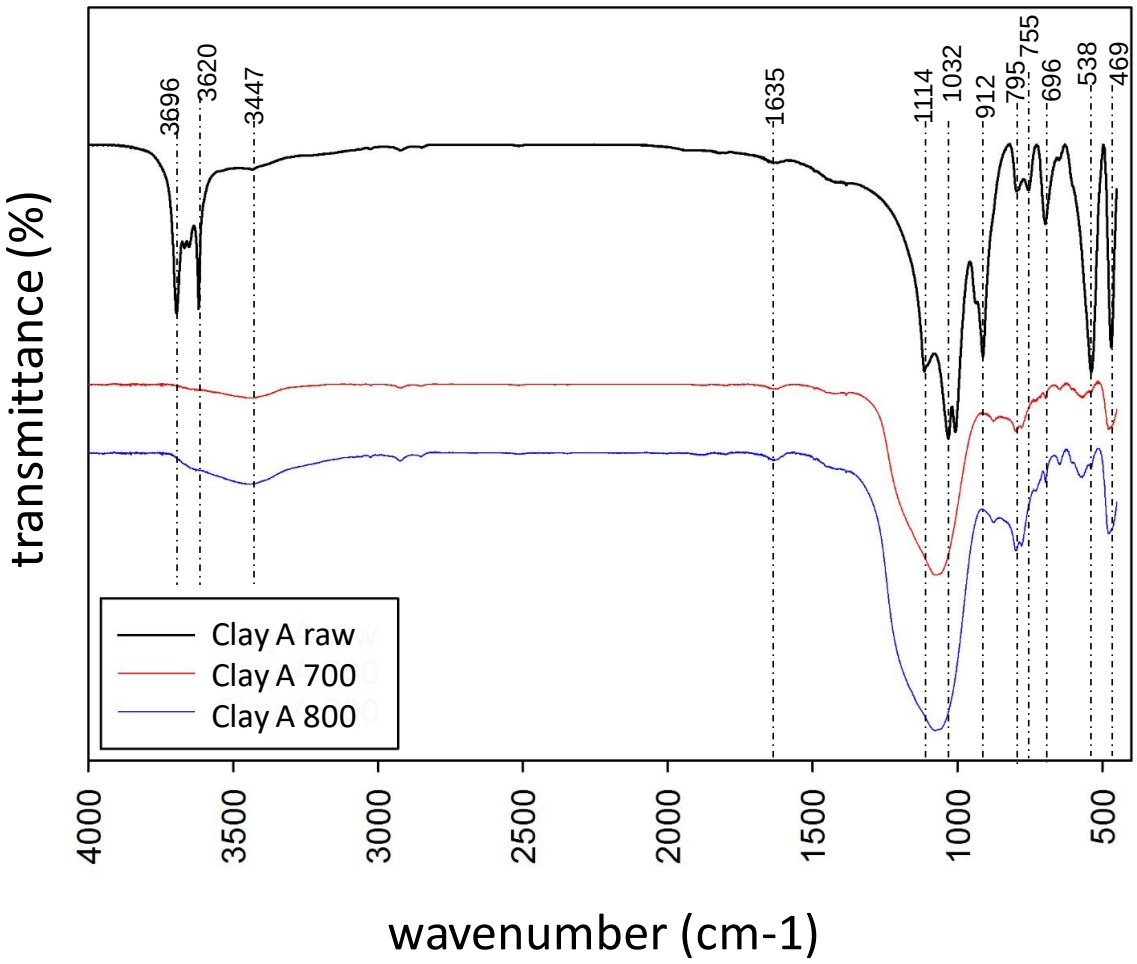

722

723 ***Figure 4: FT-IR spectra of raw and calcined (700 and 800°C) Clay A***

724

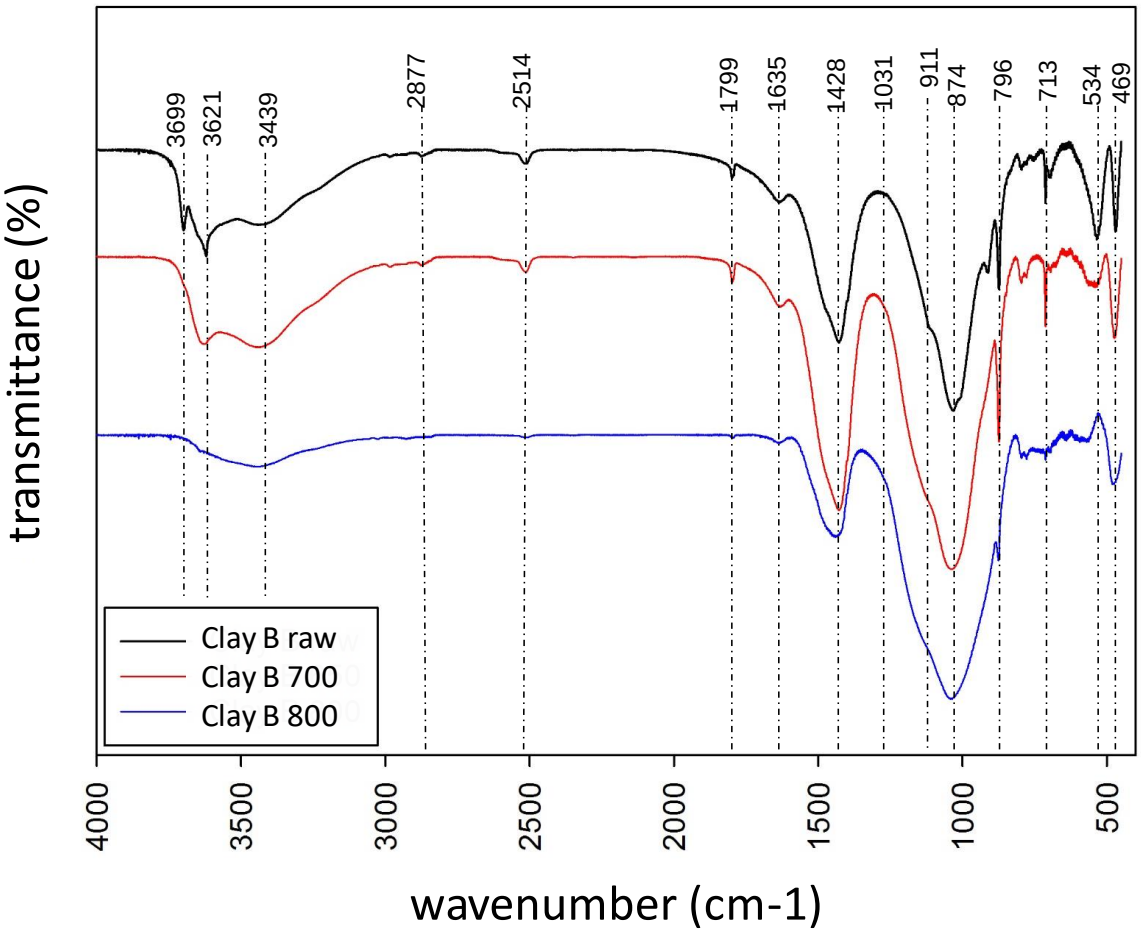

725

726 ***Figure 5: FT-IR spectra of the raw and calcined (700 and 800°C) Clay B***

727

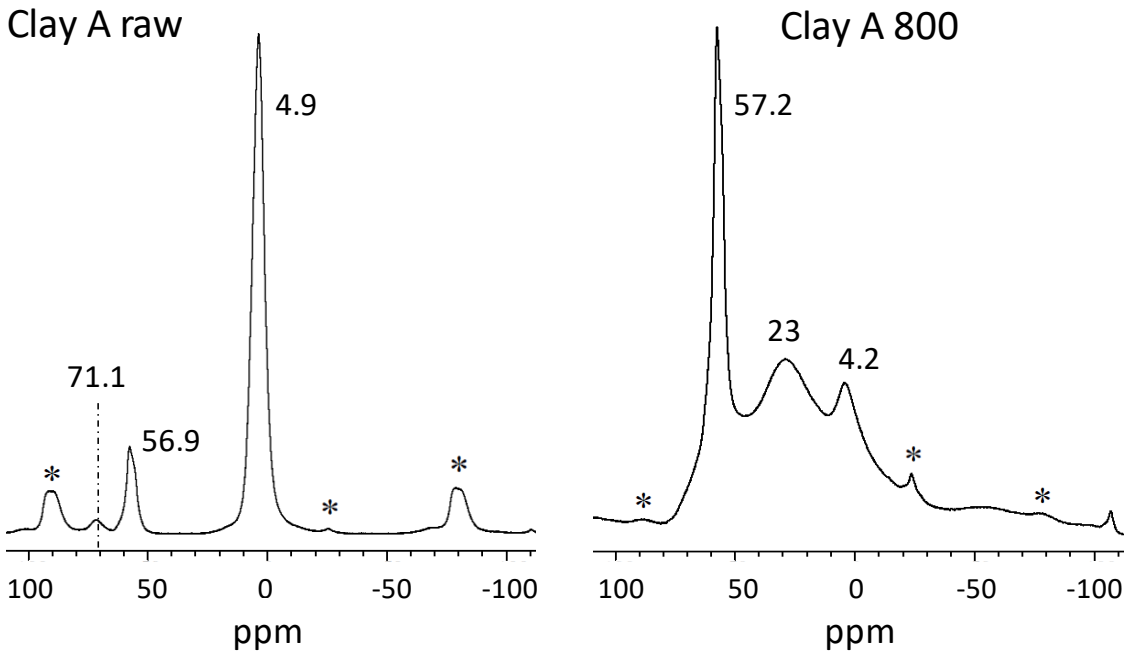

728

729 ***Figure 6: ^{27}Al MAS NMR spectra of raw and calcined Clay A***

730

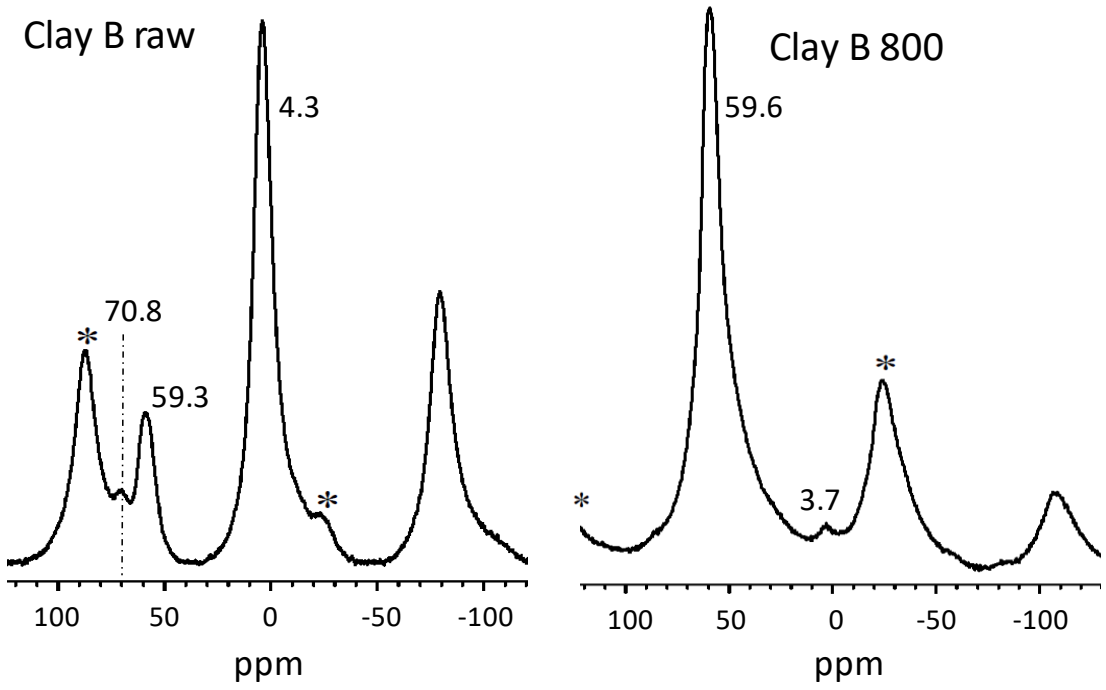

731

732 ***Figure 7: ^{27}Al MAS NMR spectra of raw and calcined Clay B***

733

734

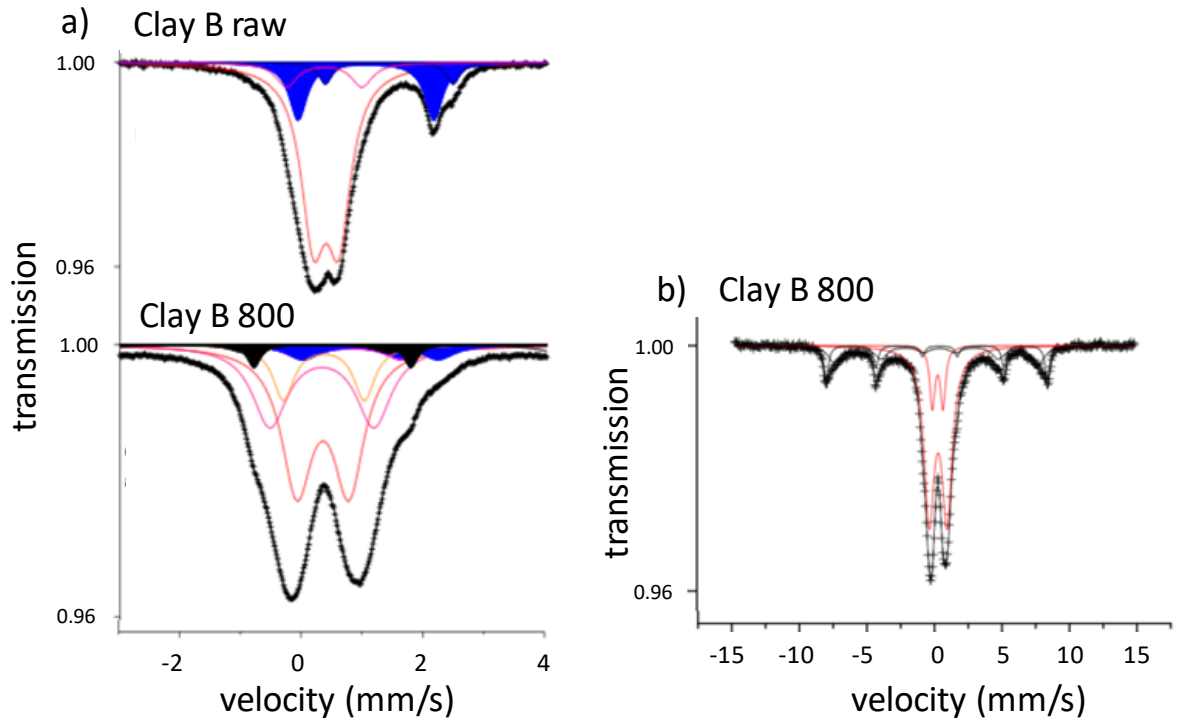

735

736 ***Figure 8: Mössbauer spectra of the raw and calcined Clay B sample with low (a) and high (b) velocity scales***

737

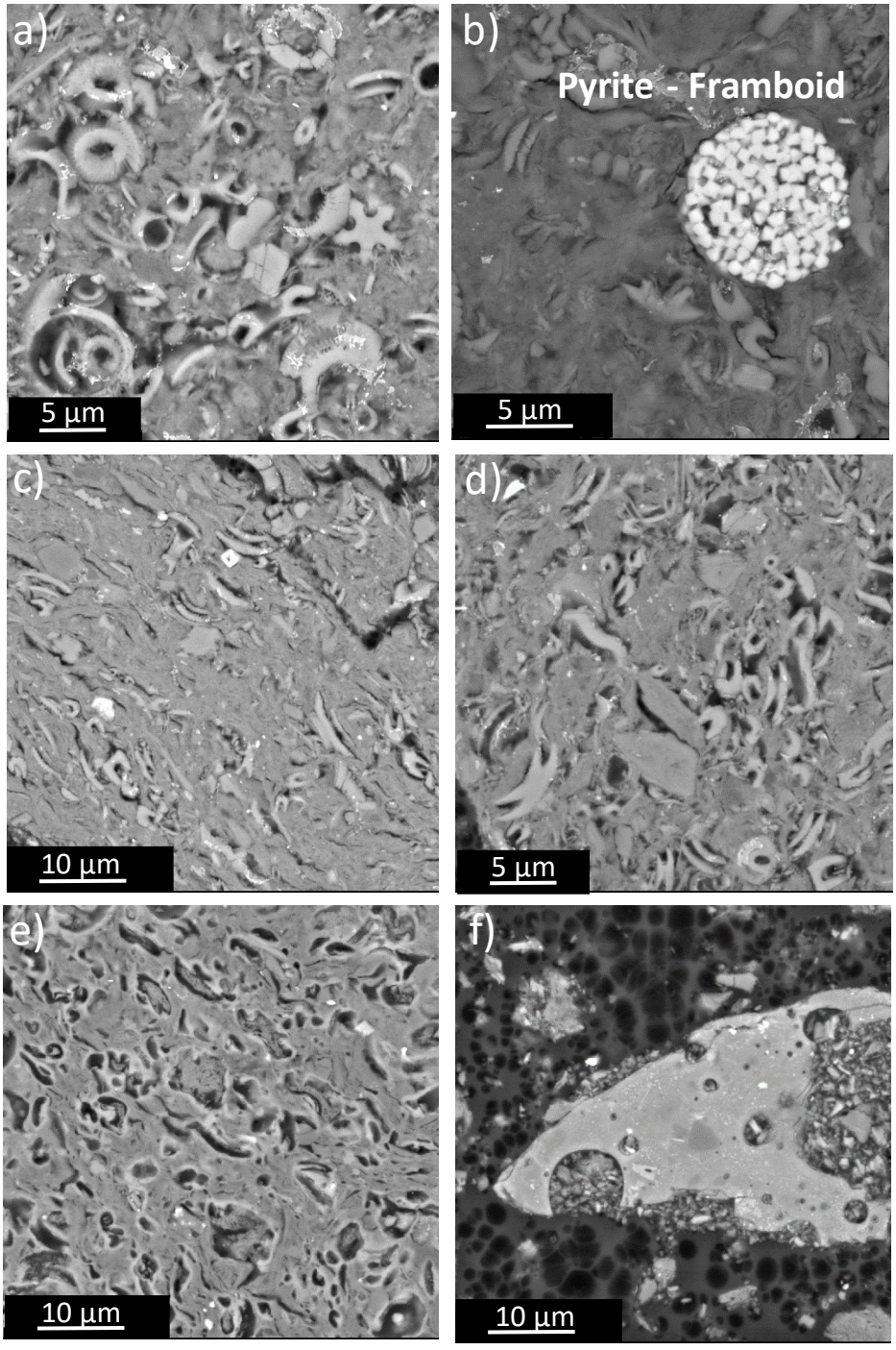

738

739 ***Figure 9: BSI images of the raw Clay A (a-b), calcined at 700 ° (c-d) and calcined at 800°C (e-f). 1 and 2 indicate points***
740 ***for WDS analysis referred to in text.***

741

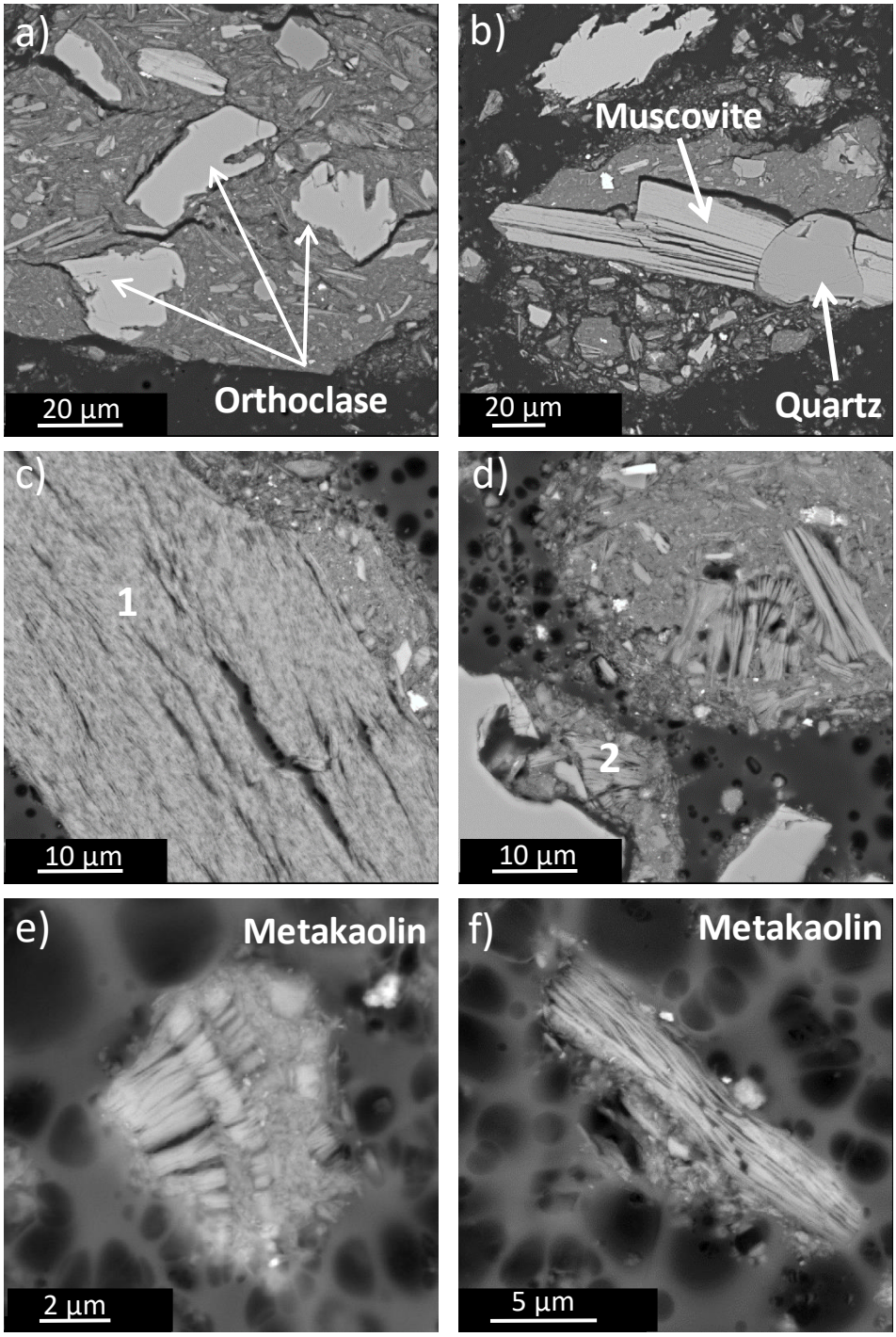

742

743 ***Figure 10: BSI images of raw Clay B (a-b), calcined at 700(c-d) and 800°C (e-f)***

744